Recent Advances and Complex Applications of the Compressible Ghost-Fluid Method

Steven Jöns, Christoph Müller, Jonas Zeifang, and Claus-Dieter Munz

Abstract In this paper, improvements to a level-set ghost-fluid scheme in a high order discontinuous Galerkin framework with finite-volume sub-cells are presented. We propose the use of a path-conservative scheme for the level-set transport in both the discontinuous Galerkin and the finite-volume framework. Additionally, improvements regarding the curvature calculation and velocity extrapolation are described. The modified scheme is validated by a comparison of shock-drop and drop-drop interaction simulations from literature.

1 Introduction

Compressible multi-phase flow is of major interest in many scientific and industrial applications. Two major concepts can be distinguished: sharp and diffuse interface methods. Popular sharp interface methods are the volume-of-fluid and the ghost-fluid method. The volume-of-fluid method is widely used for incompressible flow, but was also applied to compressible multi-phase problems, see e.g. [15]. The ghost-fluid method has been introduced by Fedkiw et al. [13] and was improved by many authors, see e.g. Liu et al. [28], [27] and Wang et al. [45]. Merkle and Rhode demonstrated a modified version, where a multi-phase Riemann problem is solved to obtain the ghost states at the interface. The concept was modified to allow approximate two-phase Riemann solvers by Fechter et al. [10–12]. The method was applied within a high order level-set ghost-fluid framework. A discontinuous Galerkin method [17] was used to transport both the bulk phases and the level-set field. Shocks as well as the

---

S. Jöns, C. Müller and J. Zeifang—These three authors contributed equally to the paper.

S. Jöns · C. Müller · J. Zeifang · C.-D. Munz (✉)
Institute of Aerodynamics and Gas Dynamics at the University of Stuttgart, Pfaffenwaldring 21, 70569 Stuttgart, Germany
e-mail: munz@iag.uni-stuttgart.de

M. L. Muñoz-Ruiz et al. (eds.), *Recent Advances in Numerical Methods for Hyperbolic PDE Systems*,
SEMA SIMAI Springer Series 28, https://doi.org/10.1007/978-3-030-72850-2_7

phase boundary between the bulk phases were captured by a finite-volume sub-cell scheme [39]. In [31], the sub-cell shock capturing method was used for the level-set transport as well. Another level-set ghost-fluid approach is based on cut-cell methods, see e.g. [32] or [44]. These approaches use similar methods to handle the level-set and the geometry calculation, however their treatment of the phase boundary is based on cut-cells. While the method of Nourgaliev et al. [32] is non-conservative like the method presented in this paper, Vahab and Miller [44] considered a conservative handling of the phase boundary.

In this paper, we focus on modifications to the interface handling of a compressible sharp interface method in order to simulate merging droplets and bubbles. The numerical framework is based on a discontinuous Galerkin flow solver with finite volume sub-cells for the bulk phases, which are coupled with a level-set ghost-fluid method. The description of the scheme will be kept short, details are described in [11] and [31]. We propose the use of a path-conservative scheme to transport the level-set field. This leads to a modified sub-cell shock capturing based on [8]. We additionally discuss novel modifications of the curvature calculation and the level-set transport, which allow the simulation of phase boundaries with high curvatures as well as topological changes. Afterwards, complex test cases are shown to validate the scheme: two cases with merging drops and two shock-drop interactions, which are compared with results from literature.

2 Governing Equations

The level-set ghost-fluid framework under consideration is a sharp interface method and assumes two distinct pure phases without a mixing zone. We model each of these bulk phases with the compressible Euler equations

$$\frac{\partial \mathbf{Q}}{\partial t} + \nabla \cdot \boldsymbol{\mathcal{F}}(\mathbf{Q}) = 0, \quad \text{with} \quad \mathbf{Q} = \begin{pmatrix} \rho \\ \mathbf{m} \\ E \end{pmatrix} \quad \text{and} \quad \boldsymbol{\mathcal{F}}(\mathbf{Q}) = \begin{pmatrix} \rho \mathbf{u} \\ \rho \mathbf{u}\mathbf{u} + \underline{\mathbf{I}} p \\ (\rho e + p)\mathbf{u} \end{pmatrix}, \tag{1}$$

with density ρ, momentum $\mathbf{m} = \rho \mathbf{u}$ and total energy $E = \rho e$ as conserved quantities. The total energy E is the sum of the internal energy per unit volume $\rho\epsilon$ and the kinetic energy $\frac{1}{2}\rho \mathbf{u} \cdot \mathbf{u}$

$$E = \rho\epsilon + \frac{1}{2}\rho \mathbf{u} \cdot \mathbf{u}, \tag{2}$$

with $\mathbf{u}$ denoting the velocity. An equation of state (EOS) has to be specified to link the pressure and the internal energy per unit mass ϵ:

$$p = p(\rho, \epsilon), \quad \epsilon = \epsilon(\rho, p). \tag{3}$$

With our framework, an arbitrary EOS can be used. Efficiency is secured by using the tabulation technique by Föll et al. [14], whereas an explicit evaluation of algebraic EOS is also possible. In this paper, we fit a stiffened gas EOS, see Saurel et al. [35], for the liquid phase and use the perfect gas law for the gaseous phase. The stiffened gas law is chosen over the Tait EOS although the latter has been found out to model water more precisely, see e.g. [34]. However, the Tait EOS simply links density and pressure. Therefore, it cannot be applied to the full compressible Euler equations directly. Following [13, 29], an additional equation for the internal energy has to be added to use it in this case. With the choice in [13] the Tait EOS can be rewritten to the form of the stiffened gas EOS. This approach was used in e.g. [20, 52] as well. For a further discussion on the use of different EOS for the modeling of water see [5, 20], and e.g. [46, 47] as exemplary applications with different EOS.

The interface between the two phases is tracked by the level-set function Φ, which is transported by a velocity field $\mathbf{s}$ according to

$$\frac{\partial \Phi}{\partial t} + \mathbf{s} \cdot \nabla \Phi = 0. \tag{4}$$

The transport velocity of the level-set function depends on the flow states at the interface $\mathbf{s} = f(\mathbf{Q}_{liq}, \mathbf{Q}_{gas})$. It is initially given on the phase boundary and is then extrapolated into the volume. In our numerical framework (Sect. 3), it is only calculated at the beginning of each time-step to reduce the complexity of the coupling between fluid motion and level-set transport. As a direct consequence, the transport velocity field is constant within each timestep and thus we can rewrite Eq. (4) to

$$\frac{\partial W}{\partial t} + \boldsymbol{\mathcal{B}}(\mathbf{x}) \cdot \nabla W = 0 \quad \text{with} \quad W = \Phi \quad \text{and} \quad \boldsymbol{\mathcal{B}}(\mathbf{x}) = \mathbf{s}. \tag{5}$$

Equation (5) is formulated in the general form of non-conservative hyperbolic equations to introduce the notation for the numerical scheme, which is discussed in Sect. 3. The root of the level-set field marks the phase interface. The level-set function initially fulfills the signed distance property. However, this property is not preserved by the level-set transport (Eq. (5)). As a result, the level-set function needs to be reinitialized. In this work, the method of choice is the solution of a Hamilton-Jacobi equation

$$\frac{\partial \Phi}{\partial t} + \operatorname{sign}(\Phi)\,(|\nabla \Phi| - 1) = 0 \tag{6}$$

as proposed in [40]. There are other approaches to reinitialize the level-set field, see e.g. [37, 43]. A beneficial aspect of level-set methods is that geometrical properties, such as normal vector $\mathbf{n}_{LS}$ and curvature κ_{LS} can be calculated directly from the level-set function by differentiation. According to [6], the level-set normal is calculated by

$$\mathbf{n}_{LS} = \frac{\nabla \Phi}{|\nabla \Phi|}. \tag{7}$$

For the calculation of the curvature the general formulation given in [6]

$$\begin{aligned}\kappa_{LS} = & \frac{\Phi_x^2 \Phi_{yy} - 2\Phi_x \Phi_y \Phi_{xy} + \Phi_y^2 \Phi_{xx}}{|\nabla \Phi|^3} + \\ & \frac{\Phi_x^2 \Phi_{zz} - 2\Phi_x \Phi_z \Phi_{xz} + \Phi_z^2 \Phi_{xx}}{|\nabla \Phi|^3} + \\ & \frac{\Phi_y^2 \Phi_{zz} - 2\Phi_y \Phi_z \Phi_{yz} + \Phi_z^2 \Phi_{yy}}{|\nabla \Phi|^3}.\end{aligned} \tag{8}$$

is preferred over the simpler formulation

$$\kappa_{LS} = \nabla \cdot \mathbf{n}_{LS}. \tag{9}$$

We found that the general formulation is beneficial to obtain stable simulations of merging droplets. A possible reason is the underresolution of the level-set field in these situations. More sophisticated algorithms for the normal and curvature calculation based on curve parametrizations are discussed e.g. in [26], but are not considered in this work due to their increased computational cost. In addition to the geometrical properties, the velocity of the level-set field **s** has to be determined as well. It is only calculated on the phase boundary and has to be extrapolated into the volume. This is typically done in a two-step procedure: First, the data is set in the neighborhood of the phase boundary. Afterwards, this initial field is extrapolated by solving the Hamilton-Jacobi equations

$$\frac{\partial s^i}{\partial \tau} + \text{sign}(\Phi)\mathbf{n}_{LS} \cdot \nabla s^i = 0 \quad i = 1, \ldots, d, \tag{10}$$

for the direction-wise components s^i of the d-dimensional velocity field **s** following [1]. This is discussed in more detail in Sect. 3.2.3.

Both the reintialization and the velocity extrapolation are only performed in a narrow, radial band around the level-set zero. Outside the narrow band the level-set function is set to the bands fixed radius and the velocity field is set to zero.

3 Numerical Method

In this section, the general numerical framework is described briefly. First, the building blocks for the method are described in Sect. 3.1. Afterwards, they are assembled in Sec. 3.2 to form the high order framework for the sharp interface simulations.

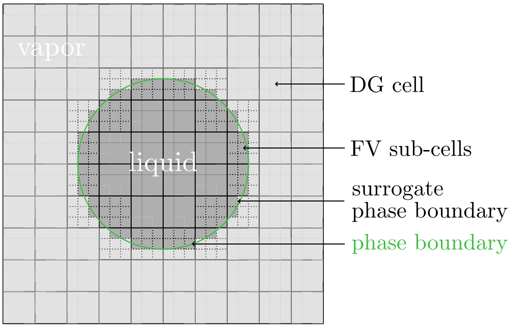

Fig. 1 Domain decomposition into liquid (dark gray) and vapor (light gray) region, using the zero position of a level-set function (green). Instead of the DG method, a FV sub-cell scheme is used in a narrow band around the resulting surrogate phase boundary.

We start by introducing basic notation. The domain $\overline{\Omega}$ is divided into a liquid region Ω^l and a vapor region Ω^v with the phase interface Γ. It holds

$$\overline{\Omega} = \overline{\Omega^l} \cup \overline{\Omega^v},\ \Omega^l \cap \Omega^v = \emptyset,\ \text{and}\ \overline{\Omega^l} \cap \overline{\Omega^v} = \Gamma.$$

Furthermore, $\overline{\Omega}$ is discretized with hexahedral elements such that

$$\overline{\Omega} = \bigcup_e \overline{\Omega_e},\ \text{and}\ \Omega_i \cap \Omega_j = \emptyset, \quad \forall i \neq j.$$

The numerical framework used in this work is based on [11] and [31]. Liquid and vapor region are both discretized with the discontinuous Galerkin method. At the phase boundary, which is defined by the zero position of a level-set function, a finite volume sub-cell scheme is applied to ensure a better representation of the surrogate phase boundary. This surrogate surface discretely represents the phase boundary and is aligned with the sub-cell interfaces. For an overview on the domain decomposition see Fig. 1.

3.1 Building Blocks for the Level-Set Ghost-Fluid Method

3.1.1 The DGSEM with Finite-Volume Sub-Cells

In this subsection, we discuss the Discontinuous Galerkin Spectral Element Method (DGSEM) [23] with finite-volume sub-cells [18, 33, 39] for hyperbolic conservation laws. We extend the DGSEM with finite-volume sub-cells to the case of hyperbolic equations with non-conservative products, following [8]. Therefore, the framework of path-conservative schemes is used [4]. In the DGSEM, the approximate solution of both the bulk phases and the level-set is described by piecewise polynomials $\mathbf{Q}_h$ and W_h of degree N, respectively. Within each element Ω_e the solutions are represented by a tensor product of nodal one-dimensional Lagrange basis functions. The basis functions are chosen to be identical to the test functions l in the weak formulations. The weak formulations for Eqs. (1) and (5) read

$$\frac{\partial}{\partial t}\int\limits_{\Omega_e} \mathbf{Q}_h l d\mathbf{x} + \oint\limits_{\partial\Omega_e} \boldsymbol{\mathcal{F}}(\mathbf{Q}_h)\cdot \mathbf{n} l ds - \int\limits_{\Omega_e} \boldsymbol{\mathcal{F}}(\mathbf{Q}_h)\cdot \nabla l d\mathbf{x} = 0, \tag{11}$$

$$\frac{\partial}{\partial t}\int\limits_{\Omega_e} W_h l d\mathbf{x} + \oint\limits_{\partial\Omega_e} \boldsymbol{\mathcal{B}}(\mathbf{x})\cdot \nabla W_h l ds + \int\limits_{\Omega_e} \boldsymbol{\mathcal{B}}(\mathbf{x})\cdot \nabla W_h l d\mathbf{x} = 0, \tag{12}$$

with the outward pointing normal vector $\mathbf{n}$. In the Euler equations, the neighboring elements are coupled by a numerical flux function $\boldsymbol{\mathcal{F}}^*(\mathbf{Q}_h^-, \mathbf{Q}_h^+)\cdot\mathbf{n} \approx \boldsymbol{\mathcal{F}}(\mathbf{Q}_h)\cdot\mathbf{n}$. We use the HLLC [42] and the HLLE [9] Riemann solver. For the level-set transport equation, the path-conservative jump term $\boldsymbol{\mathcal{D}}^*(W_h^-, W_h^+)\cdot\mathbf{n} \approx \boldsymbol{\mathcal{B}}(\mathbf{x})\cdot\nabla W_h$ has to be approximated. We use the path-conservative Rusanov Riemann solver [8]

$$\boldsymbol{\mathcal{D}}^*(W_h^-, W_h^+)\cdot\mathbf{n} = \frac{1}{2}\left(\widetilde{\boldsymbol{\mathcal{B}}}\cdot\mathbf{n} - s_{max}\underline{\mathbf{I}}\right)\left(W_h^+ - W_h^-\right) \tag{13}$$

with the maximal signal speed

$$s_{max} = \max\left(|\mathbf{s}^+\cdot\mathbf{n}|, |\mathbf{s}^-\cdot\mathbf{n}|\right). \tag{14}$$

The superscript $(\cdot)^-$ identifies the value inside the current cell and the superscript $(\cdot)^+$ identifies the value outside the current cell. To approximate the Roe type matrix $\widetilde{\boldsymbol{\mathcal{B}}}$ we substitute the spatial dependency of $\boldsymbol{\mathcal{B}}$ on $\mathbf{x}$ with a dependency on W_h. In general, this is not valid as the advection field is a function of space. However, the level-set variable Φ carries the signed-distance property. Hence, in a 1D Riemann problem it is possible to transform the spatial dependency to a dependency on the level-set field. This enables to approximate $\widetilde{\boldsymbol{\mathcal{B}}}$ by integrating along a linear path $\Psi(W_h^-, W_h^+, b)$, with $b \in [0, 1]$ between W_h^- and W_h^+ as

$$\widetilde{\boldsymbol{\mathcal{B}}}\cdot\mathbf{n} \approx \int\limits_0^1 \boldsymbol{\mathcal{B}}(\Psi(W_h^-, W_h^+, b))\cdot\mathbf{n} db, \quad \Psi(W_h^-, W_h^+, b) = W_h^- + b(W_h^+ - W_h^-). \tag{15}$$

We evaluate the path numerically with the trapezoidal rule and obtain

$$\widetilde{\boldsymbol{\mathcal{B}}}\cdot\mathbf{n} \approx \frac{\boldsymbol{\mathcal{B}}(W_h^-) + \boldsymbol{\mathcal{B}}(W_h^+)}{2}\cdot\mathbf{n}. \tag{16}$$

The volume terms in Eq. (11) and Eq. (12) can be calculated directly from $\mathbf{Q}_h$ and W_h. The derivatives of the test function and the solution can be calculated by derivating the respective polynomial.

The main idea of the DGSEM is to choose the same $N + 1$ Legendre-Gauss points for both the numerical integration and the interpolation of the solution. This reduces the number of operations per degree of freedom and increases the efficiency. In addition, the multi-dimensional operator simplifies to a subsequent application of the one-dimensional operator. Details on the implementation can be found in [2, 24] and [17].

The finite-volume formulations of Eqs. (1) and (5) are a special case of the weak formulations Eqs. (11) and (12). If both the solution and the testfunction are chosen out of the space of piecewise constant polynomials, e.g. $l = 1$, Eqs. (11) and (12) simplify to the finite-volume methods

$$\frac{\partial}{\partial t}\int\limits_{\Omega_e} \mathbf{Q}_h d\mathbf{x} + \oint\limits_{\partial\Omega_e} \boldsymbol{\mathcal{F}}^*(\mathbf{Q}_h^-, \mathbf{Q}_h^+) \cdot \mathbf{n} ds = 0, \tag{17}$$

$$\frac{\partial}{\partial t}\int\limits_{\Omega_e} W_h d\mathbf{x} + \oint\limits_{\partial\Omega_e} \boldsymbol{\mathcal{D}}^*(W_h^-, W_h^+) \cdot \mathbf{n} ds = 0. \tag{18}$$

We combine the DGSEM and FV approach to capture discontinuities in the high order DGSEM solution, which would otherwise lead to oscillations. In the Euler equations, shocks and the phase boundary have to be captured. For the level-set equation, the edge of the narrow band requires stabilization. In addition, areas with a high curvature with respect to the grid resolution are troublesome. This can be resolved by either a grid refinement or the sub-cell scheme. Additional problems occur if level-set contours merge, e.g. merging drops. In this case, the process has to be captured by a low order scheme like the sub-cell approach. For the sub-cell method we formulate an a priori limiter following [39] in contrast to the a posteriori limiter in [8]. The biggest advantage is a reduction in computational cost, since only one operator is evaluated in each cell. A disadvantage is that there is no guarantee of a stable solution. We combine multiple approaches to identify trouble cells of the DGSEM method: First, a modal indicator following [18, 33] is used to detect strong gradients in the solution of the Euler equations and the edge of the narrow band in the solution of the level-set function. Details on modifications and the implementation can be found in [38]. Second, the position of the level-set zero is used to capture the phase boundary in the Euler equations. Finally, we detect zones in which two phase boundaries meet, e.g. the merging of two droplets. Details are discussed in Sect. 3.2.4. After the troubled cells are identified, the polynomial solution is switched to a finite-volume representation. If the cells are no longer problematic they are switched back. The switch upholds

$$\int_{\Omega_e} \mathbf{U} d\mathbf{x} \equiv \int_{\Omega_e} \mathbf{U}_{DG} d\mathbf{x} = \int_{\Omega_e} \mathbf{U}_{FV} d\mathbf{x} \quad \mathbf{U} = \mathbf{Q}, W \tag{19}$$

and hence is conservative. It can be formulated as a matrix vector multiplication with an integration matrix $\mathcal{V}$

$$\mathcal{V}\mathbf{U}_{DG} = \mathbf{U}_{FV} \quad \mathbf{U} = \mathbf{Q}, W. \tag{20}$$

The polynomial representation has $(N+1)^d$ degrees of freedom, with d denoting the number of dimensions. For the finite-volume method, we choose to use $(N+1)^d$ equidistantly distributed finite-volume sub-cells. This choice allows the use of the same data structure and hence an easy implementation. For the Euler equation, the finite-volume scheme is extended to a second order TVD scheme. The coupling between the DGSEM and the sub-cells occurs via the surface terms on the element boundaries. The fluxes and jump terms are evaluated in the finite-volume discretization and then projected to the polynomial discretization for the DG elements. The scheme handles discontinuities well, since it switches to the finite-volume representation if necessary. Its use of finite-volume sub-cells intrinsically leads to a grid refinement, which prevents a strong loss of accuracy.

We want to highlight some advantages of the novel approach for the level-set transport compared with the previously discussed approach in [12, 31]. There, Eq. (5) is used in a divergence form with a source term

$$\frac{\partial \Phi}{\partial t} + \nabla \cdot (\mathbf{s}\Phi) = \Phi \nabla \cdot \mathbf{s}. \tag{21}$$

In the incompressible case the right hand side of Eq. (21) is zero since the velocity field is divergence free ($\nabla \cdot \mathbf{s} = 0$), see e.g. [16, 30]. However, in the compressible case this term needs to be discretized.

The novel path-conservative scheme has two advantages: First, the DGSEM and finite-volume sub-cell scheme are derived from the same weak formulation and solve the same equation on the discrete level. In this sense, they are consistent. If Eq. (21) is solved instead, $\nabla \cdot \mathbf{s} \neq 0$ still holds discretely for the discontinuous Galerkin method. However, in the finite-volume scheme $\mathbf{s}$ is discretized with constant polynomials and thus $\nabla \cdot \mathbf{s} = 0$. As a result both schemes solve different equations although they are formally derived from the same weak formulation. Secondly, the time-step is only limited by the eigenvalues of the hyperbolic transport, which is the process of interest. If Eq. (21) is solved, the source term might be stiff. In this case the eigenvalues of the source are larger than those of the hyperbolic transport. This leads to smaller time-steps and thus higher costs of the numerical simulations.

3.1.2 Time Discretization

For the temporal discretization of the level-set transport and the Euler equations we either use a fully explicit 4^{th} order Runge-Kutta (RK) scheme from [3] or an implicit-explicit 4^{th} order Runge-Kutta scheme by Kennedy and Carpenter [21]. The goal of implicit-explicit time discretization is to overcome the severe time step restriction of explicit schemes at low Mach numbers. Hence, we treat the Euler equations with an implicit scheme and the level-set transport with an explicit scheme. For solving the arising non-linear equation system of the implicit part we rely on a matrix-free Newton-GMRES approach [22] as it is applied to the DGSEM formulation in [50, 51] and extend it to the mixed DG-FV ghost-fluid formulation. More details about this time discretization will be presented in a follow-up publication.

3.2 The Level-Set Ghost-Fluid Method

The numerical methods described above are the building blocks of the present level-set ghost-fluid framework. In the following, we describe the necessary steps to assemble the framework.

3.2.1 Algorithmic Details of the Level-Set Ghost-Fluid Method

We follow the approach in [11] for the development of our method. It consists of the repetition of the following steps:

1. The RK-DGSEM/RK-FV solver is used to advance the level-set field and the Euler equations for the pure phases in time.
2. The level-set function is reinitialized.
3. Depending on the level-set root, the domain Ω is decomposed into Ω^l and Ω^v along the boundaries of the finite-volume sub-cells using already existing physical states and ghost states. This creates a surrogate phase boundary Γ^s.
4. The DG-FV distribution of both the Euler equations and the level-set is updated based on modal smoothness indicators and geometrical information of the level-set function.
5. The normal vector at the phase interface and the curvature are calculated.
6. The boundary conditions at the surrogate phase boundary and its velocity are calculated with a two-phase Riemann solver, the so called HLLP Riemann solver [11, 36]. It models surface tension with a jump term across the phase boundary and provides both fluxes for each phase as well as the velocity of the phase boundary.
7. The interface velocity is then extrapolated into the volume to obtain a velocity field for the level-set transport.

Before the initial time-step is executed, the above mentioned procedure has to be done once without step 1. Additionally, step 6 is applied in each Runge-Kutta stage. The presented level-set ghost-fluid algorithm does not guarantee conservation due to two reasons. First, the fluxes at the surrogate phase boundary may be distinct to ensure a stable two-fluid simulation. Secondly, the state of cells which change from the liquid into the vapor domain and vice versa are replaced with their respective ghost state in step 3. For more details about the method the reader is referred to [31].

3.2.2 Calculation of Derivatives: The Level-Set Normal Vector and Curvature

The normals and the curvature are calculated by first transforming the level-set solution to the finite-volume sub-cell representation via Eq. (20) and secondly calculating the derivatives of the level-set function with a 5th order WENO stencil as proposed in [10]. The same operator is applied again to the components of $\nabla\Phi$ to obtain the second order derivatives of the level-set field. With these gradients we then evaluate Eq. (7) and Eq. (8) to calculate normal vectors and curvature of the level-set function. We additionally limit the curvature by an upper bound that depends on the grid resolution, which we characterize by $r^{min} = \min(V_{FV})^{1/d}$. Thereby, V_{FV} is the volume of a finite-volume sub-cell. With this we can define

$$|\kappa_{LS}|^{max} = \frac{d-1}{2r^{min}} = \frac{d-1}{2\min(V_{FV})^{1/d}}, \tag{22}$$

as the maximum absolute value of the curvature, which can be resolved by the grid assuming a safety factor of 0.5.

3.2.3 Solution of Hamilton-Jacobi Equations: Reinitialization and Velocity Extrapolation

Two sets of Hamilton-Jacobi equations need to be solved: the reinitialization equation Eq. (6) and the equations for the velocity extrapolation Eq. (10). Each set of equations is solved with a 5th order WENO scheme [19] in combination with a third order order low storage Runge-Kutta method with three stages [48]. For the velocity extrapolation an additional step is necessary. The solution of the two-phase Riemann problem gives a transport velocity on the cell edges that form the surrogate phase boundary. This velocity can be directly copied to the neighboring finite-volume sub-cells. If a sub-cell is involved in more than one two-phase Riemann problem, we average the velocities. In the direct neighbors of the surrogate phase interface, the velocity is fixed. In all other cells within the narrow band, we solve Eq. (10) to obtain a smooth velocity field.

3.2.4 Specific Modifications of the Algorithm for Simulating Merging Droplets

If topological changes are simulated, e.g. merging droplets, special attention has to be payed in regions where those topological changes take place. In the following we detail the two necessary modifications.

In a first step, we have to ensure that we capture topological changes with the finite-volume sub-cell framework, since they are associated with discontinuities in the level-set field. We use the topological information that is available through the sign of the level-set function. Therefore, we switch the level-set solution to the finite-volume sub-cell discretization in each element. Afterwards, we evaluate the level-set sign line-wise in all spatial directions. If the sign changes more than once, the DG element contains a topological change which has to be captured with the sub-cell approach. In a second step, we have to identify the specific sub-cells that are involved in the topological change. We check the number of two-phase Riemann problems a sub-cell is involved in. If a sub-cell is affected by more than one two-phase Riemann problem per direction it is identified as a potential *merge cell* ($\mathcal{I}_{\text{topo}} = 1$). In those cells, the advection velocity cannot be determined by averaging, cf. Sect. 3.2.3. The use of the advection velocity in the *merge cells* is avoided by introducing a specific form of the path-conservative jump term. Summarizing Eqs. (13)-(16), the path conservative jump term $\mathcal{D}^*(W_h^-, W_h^+)$ for the transport of the level-set field Eq. (5) is

$$\mathcal{D}^*(\Phi^-, \Phi^+) = \frac{1}{4}((s^+ + s^-) - 2\ \max\left(|s^+|, |s^-|\right))(\Phi^+ - \Phi^-), \tag{23}$$

where the velocities s^+, s^- are selected via

$$\begin{aligned} s^- &= \mathbf{s}^- \cdot \mathbf{n},\ s^+ = \mathbf{s}^+ \cdot \mathbf{n} \ \text{ if } \ \mathcal{I}^-_{\text{topo}} = \mathcal{I}^+_{\text{topo}},\\ s^- &= \mathbf{s}^- \cdot \mathbf{n},\ s^+ = \mathbf{s}^- \cdot \mathbf{n} \ \text{ if } \ \mathcal{I}^-_{\text{topo}} = 0,\ \mathcal{I}^+_{\text{topo}} = 1,\\ s^- &= \mathbf{s}^+ \cdot \mathbf{n},\ s^+ = \mathbf{s}^+ \cdot \mathbf{n} \ \text{ if } \ \mathcal{I}^-_{\text{topo}} = 1,\ \mathcal{I}^+_{\text{topo}} = 0. \end{aligned} \tag{24}$$

Hence, the transport velocity is chosen according to the $\mathcal{I}_{\text{topo}}$ identifier. This procedure ensures that the velocity for the level-set transport is taken only from cells that are not involved in a topological change.

4 Numerical Results

In this section we apply the numerical framework to test problems in the low and high Mach number regime. First, we look at two droplets in a gas with a linear velocity profile to evaluate the accuracy of the curvature calculation. Secondly, a simulation of two merging droplets with a Weber number of $\text{We} = 2.2$ is performed. Afterwards, two shock-drop interactions with a shock Mach number of $\text{M}_s = 1.47$ and Weber numbers of $\text{We} = 7339$ and $\text{We} = 12$ are simulated and compared to results from literature.

4.1 Drop Collision in Linear Velocity Profile

The first testcase is an adaption from [25] in which a drop collision in a shear layer has been described. Since we only consider inviscid fluids in this paper, we have slightly

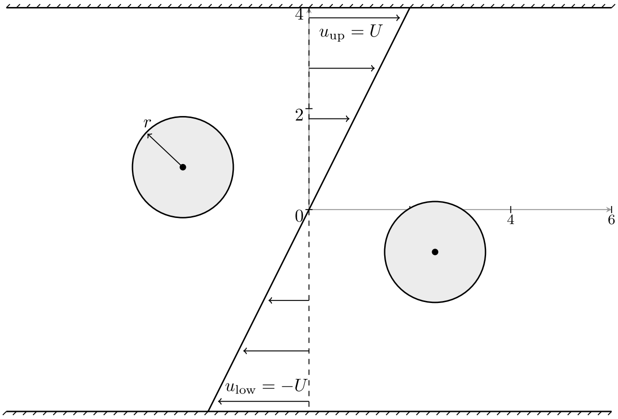

Fig. 2 Computational setup for a drop collision in a gas with a linear velocity profile. The upper and lower boundaries are slip walls whereas the left and right boundaries are periodic. The domain is discretized with 90 × 60 4^{th} order elements coupled with a HLLC Riemann solver.

Table 1 Initial conditions and material parameters for the drop collision in a linear velocity profile.

	p_0	ρ_0	γ	p_∞	σ
Gas phase	71.43	1.0	1.4	0	–
Liquid phase	81.43	1.0	7.15	3307	10

altered the test case into a collision of two drops emerged in a gas with a linear velocity profile. It allows to benchmark the curvature calculation during the merging process. It is a difficult test, since the droplets have only a small relative velocity in normal direction. The setup is visualized in Fig. 2 with the following parameters: radius $r = 1$, position of the left drop $(-2.5, 0.84)$, position of the right drop $(2.5, -0.84)$ and maximum velocity $U = 1$. The initial conditions and material parameters are given in Table 1. For the time discretization an explicit 4^{th} order Runge-Kutta scheme with CFL $= 0.3$ is used. If the static capillary time step restriction is calculated as in [7], the time-step is limited by the wave propagation of the acoustic waves. The ratio of capillary to accoustic time-step is $\Delta t^{\text{capillary}} / \Delta t^{\text{acoustic}} \approx 24$.

In Fig. 3 the temporal evolution of the phase boundary during a collision is visualized. Due to the linear velocity profile, the drops are deformed as they approach each other. The distance between the two drops shrinks until it can no longer be resolved by the grid. At this instance the drops merge. We observe two merges at two different positions that happen almost at the same time. They enclose a vapor bubble, which vanishes quickly due to its underresolution. Afterwards, a wave moves along the drop surface and changes the droplets shape towards a spherical form. The same qualitative behavior is observed in [25]. We conclude that our numerical framework is suitable to simulate merge phenomena.

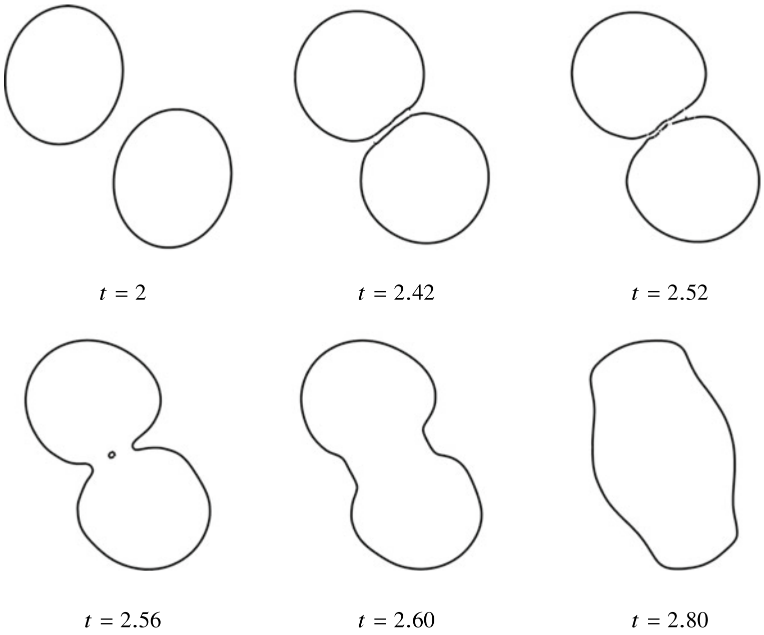
$t = 2$ $t = 2.42$ $t = 2.52$

$t = 2.56$ $t = 2.60$ $t = 2.80$

Fig. 3 Temporal evolution of the phase boundary for the drop collision in linear velocity profile. Due to inertial forces the drops are deformed as they approach each other. Then they merge and form a single drop.

Table 2 Initial conditions and material parameters for collision of liquid ethanol droplets in air.

	p_0[bar]	ρ_0[kg m^{-3}]	γ[$-$]	p_∞[bar]	σ[kg s^{-2}]
Air	1.0	1.226	1.4	0	–
Ethanol$_l$	1.11375	791	1.208	8466.14	2.275

4.2 Droplet Collisions with $\mathbf{We}_c = 2.2$

In a next step, we apply our framework to a binary droplet collision. Inspired by [41], we simulate ethanol droplets in air with a collision Weber number of $\mathrm{We}_c = 2.2$, being defined as

$$\mathrm{We}_c = \frac{\rho_l U_c^2 d}{\sigma}, \tag{25}$$

with the liquid density ρ_l, the droplet diameter d and the relative velocity of the droplet U_c. The initial conditions and material parameters are summarized in Table 2.

Both drops have a radius of $r = 0.2$ mm. Initially, they are seperated by a distance of $2.5r$. The droplets are initialized with a vertical velocity of $v^{(1)} = 2.0\frac{\mathrm{m}}{\mathrm{s}}$ and

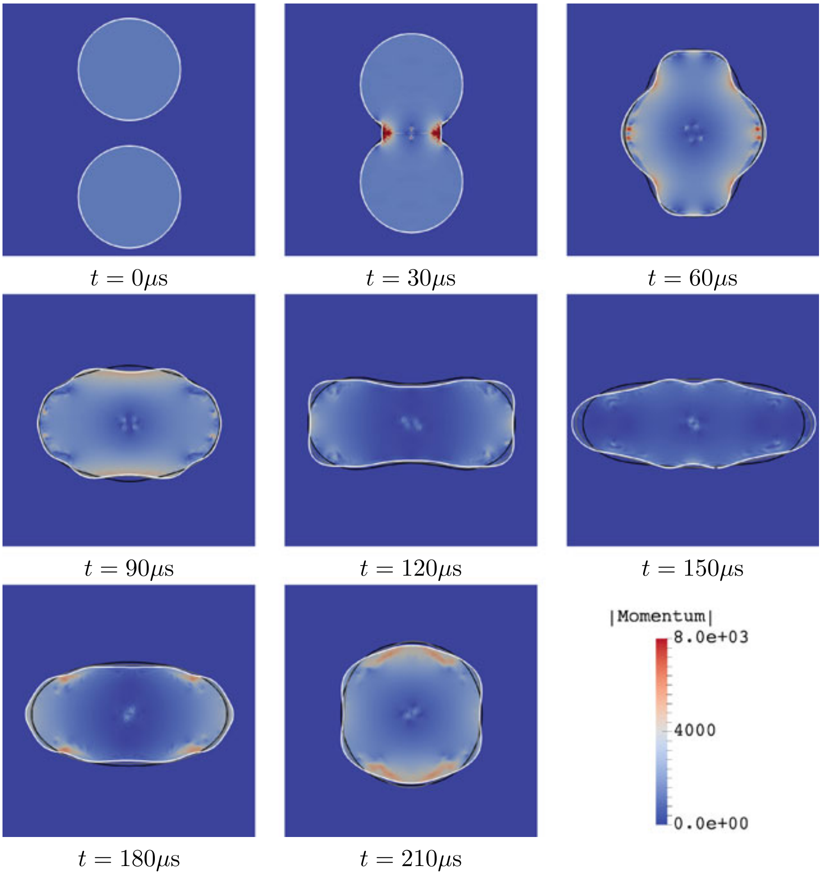

$t = 0\mu\mathrm{s}$ $t = 30\mu\mathrm{s}$ $t = 60\mu\mathrm{s}$

$t = 90\mu\mathrm{s}$ $t = 120\mu\mathrm{s}$ $t = 150\mu\mathrm{s}$

$t = 180\mu\mathrm{s}$ $t = 210\mu\mathrm{s}$

Fig. 4 Temporal evolution of the phase boundary (white line) and the absolute value of the momentum for the drop collision with $\mathrm{We}_c = 2.2$, choosing 128^2 elements with $N = 4$ for the spatial resolution. The gray and the black line indicate the phase boundary of the simulations with 64^2 and 32^2 elements, respectively.

$v^{(2)} = -2.0\frac{\mathrm{m}}{\mathrm{s}}$ to obtain a collision Weber number of $\mathrm{We}_c = 2.2$. Following [41], we expect coalescence of the two droplets and an oscillation of the remaining single drop. Diverging from the setup in [41] we do not use radial coordinates and neglect viscous effects. The domain $\Omega = [-0.75mm, 0.75mm]^2$ is discretized with three different resolutions with 32^2, 64^2 and 128^2 elements. A polynomial degree of $N = 4$ and the HLLC Riemann solver is used. A 4^{th} order implicit-explicit scheme, see Sect. 3.1.2, is used for the time discretization. For this setup, we achieve a speed-up of approximately 4 compared to the fully explicit scheme. Due to the low Mach number, we can choose a time-step that is approximately 25 times larger than for the explicit scheme with a CFL number of CFL = 0.8. Still, the acoustic waves are the

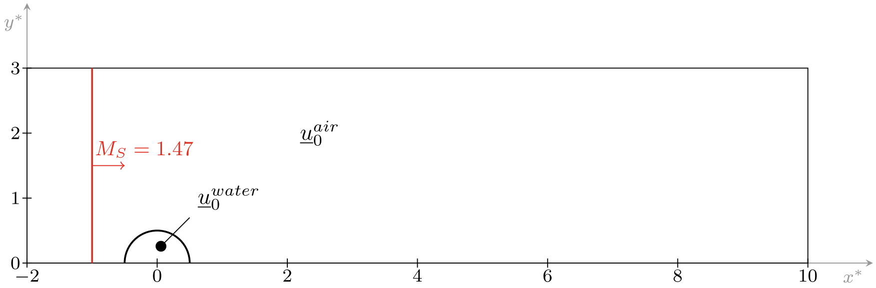

Fig. 5 Computational setup for the shock droplet interaction assuming symmetric conditions. The shock is depicted in red.

fastest characteristics as the ratio $\Delta t^{\text{capillary}}_{\text{explicit}} / \Delta t^{\text{acoustic}}_{\text{explicit}}$ ranges from ≈ 75 to ≈ 150 for the three different spatial resolutions.

In Fig. 4, the temporal evolution of the absolute value of the momentum for the discretization with 128^2 elements is visualized. Additionally, the phase boundary for the simulations with 32^2, 64^2 and 128^2 elements is indicated with a black, a gray and a white line, respectively. We observe the expected behavior qualitatively. A quantitative comparison with [41] is not possible due to the neglect of viscous and three-dimensional effects. A particular consequence of the inviscid flow model is the occurence of further deformations of the phase interface under grid refinement. The only stabilizing mechanism is the numerical viscosity, which decreases as the grid resolution increases. A convergent behavior of the observed phenomena should occur if viscous effects are considered.

4.3 Shock-Droplet Interaction

In the following, we simulate 2D shock-droplet interactions at two different Weber numbers, We $=$ 7339 and We $=$ 12. The numerical setup is taken from Winter et al. [49] and is visualized in Fig. 5. However, we neglect viscous effects. We initialize a water droplet at rest surrounded by air at $x = 0$. A right moving shock wave with a Mach number of $\mathrm{M}_s = 1.47$ is positioned at $x = -D_0$. The initial droplet diameter is chosen as $D_0 = 1m$. The lower domain boundary is set as a symmetry plane. On the left, Dirichlet boundary conditions impose the initial conditions onto the boundary. The remaining boundaries are treated as supersonic outflows. Since both M_s and We are higher than in the test cases considered in Sects. 4.1 and 4.2, the capillary time-step restriction is not considered here. The domain $\Omega = [-2D_0, 10D_0] \times [0, 3D_0]$ is discretized with 512×256 DG elements. For this testcase we use the HLLE Riemann solver, explicit 4^{th} order Runge-Kutta time integration and a polynomial degree of $N = 3$. Initial conditions and material parameters for both considered cases are given in Table 3. The droplet is initialized in mechanical equilibrium with the surrounding

Table 3 Initial conditions and material parameters for the shock-droplet interaction.

	p_0[bar]	ρ_0[kg m^{-3}]	γ[−]	p_∞[bar]	σ[Nm^{-1}]
Air	1.01325	1.204	1.4	0	–
Water (SIE)	1.01355	1000	6.12	3430	15.1571
Water (RTP)	1.19865	1000	6.12	3430	9269.85

air. The pressure difference between droplet and air is given by the Young-Laplace Law. For the comparison with the literature, the non-dimensional time t^* is defined as

$$t^* = \frac{t}{\frac{D_0}{u_s}\sqrt{\frac{\rho_L}{\rho_s}}}, \tag{26}$$

with u_s denoting the post shock velocity and ρ_s the post shock density.

As in Winter et al. [49], we considered two breakup regimes: the shear induced entrainment (SIE) regime and the Rayleigh-Taylor piercing (RTP) regime. For the SIE case, We = 7339, we show the results at the time instances $t^* = 0.25$, $t^* = 0.75$ and $t^* = 1.5$ in Fig. 6. After the shock impinges on the droplet, the surrounding flow deforms the droplet's surface and a complex vortex system is generated in the wake. The two disconnected ligaments at $t^* = 1.5$ stem from the fact that part of the interface has already left the domain. Comparing with the results of Winter et al. [49], the deformations are very similar in the early stages of the simulation. At later stages, differences become more and more apparent. These stem from the neglect of viscous effects in the presented results. The inclusion of viscosity at the interface by Winter et al. [49] produces a smoother droplet surface and a postponed breakup. This can be observed by comparing the time instance $t^* = 1.5$ from Fig. 6 with their results. Nevertheless, this testcase displays the capability of the proposed framework to capture strongly deformed interfaces. An inclusion of viscous effects will be considered in future work.

Next, we consider the RTP case, We = 12. Here, viscous effects are negligible. Results for the non-dimensional time instances $t^* = 0.25$, $t^* = 0.75$ and $t^* = 1.5$ can be seen in Fig. 7. Similar to the SIE case, the droplet deforms after the shock impingement. However, due to the larger surface tension forces, the droplet maintains a more compact form in contrast to the case with a higher We number. Comparing with the results shown in [49], both simulations show a good agreement in the predicted droplet shape. These results demonstrate that our method allows to simulate complex high Mach number settings.

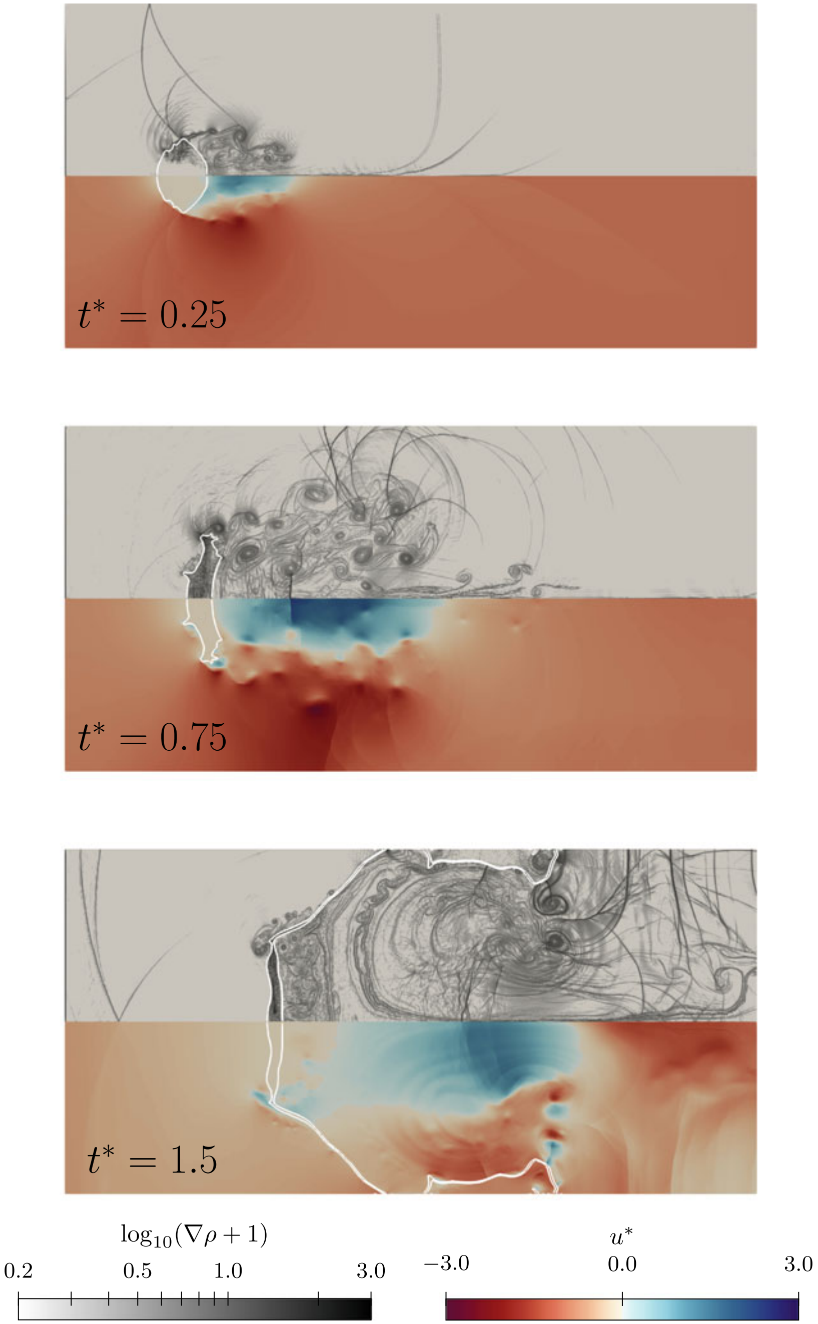

Fig. 6 Numerical Schlieren image(top) and non-dimensional streamwise velocity(bottom) $u^* = u/u_s$ for the SIE case at different time instances. The phase interface is depicted in white.

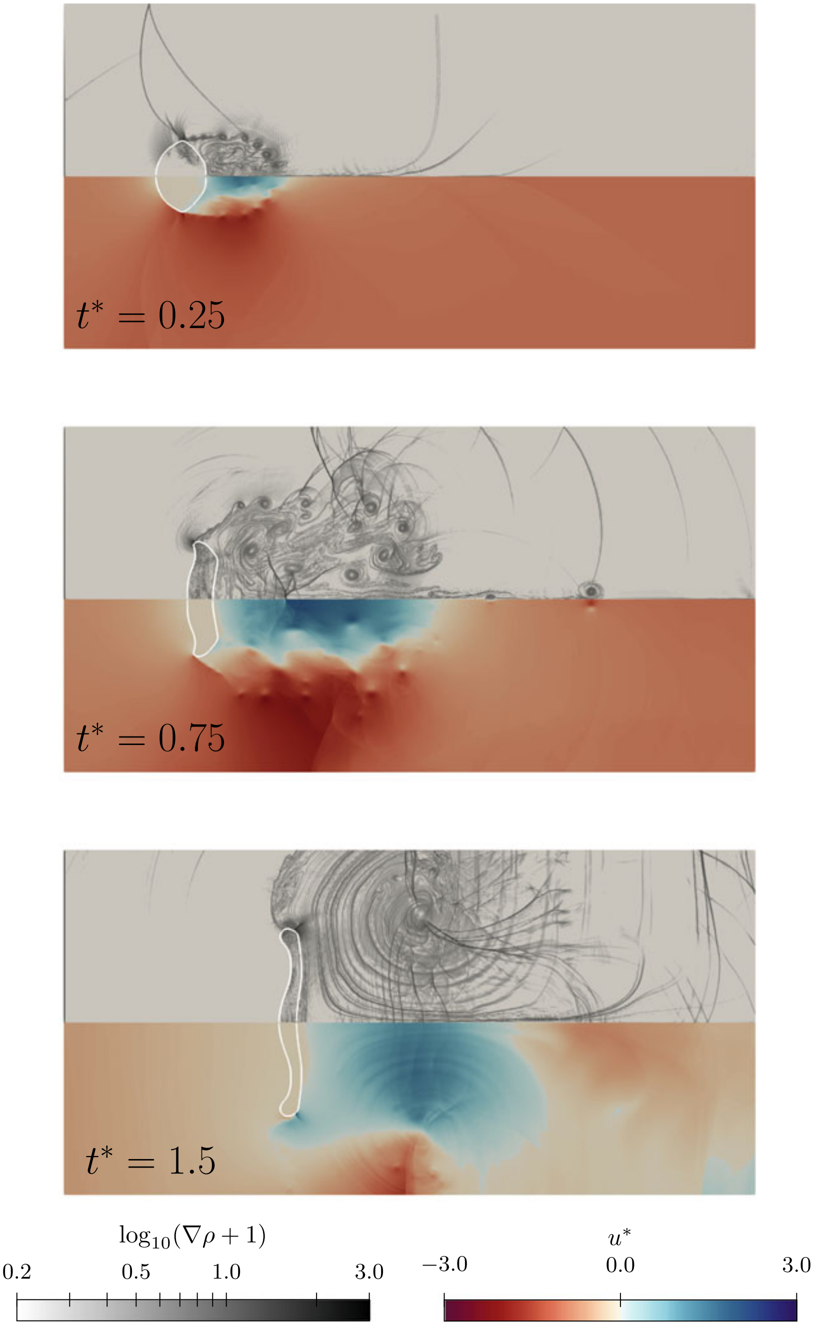

Fig. 7 Numerical Schlieren image(top) and non-dimensional streamwise velocity(bottom) $u^* = u/u_s$ for the RTP case at different time instances. The phase interface is depicted in white.

5 Conclusion

In this paper we provided an overview over a level-set ghost-fluid framework for sharp interface multi-phase flow simulations based on the work in [10] and [31]. We discussed an improved finite-volume sub-cell scheme for the level-set equation based on path-conservative schemes. In addition, two changes in the curvature calculation were presented. At first, the general second derivative of the level-set was used. Secondly, we introduced an upper bound of the curvature value, depending on the size of the grid elements, limiting the curvature by the grid resolution. At last, we discussed a necessary modification of the level-set transport to capture merging phenomena. We avoided the use of the transport velocity in the *merge cells* since it cannot be defined properly.

We showed that these modifications allow the simulation of merging drops with surface tension in two settings: drops in a gas with a linear velocity profile and colliding drops. Afterwards we showed that complex shock-drop interactions are also well within the capabilities of the framework. The modifications allowed the resolution of very fine two-phase structures with respect to the grid size and ensured a stable simulation. We currently work on an extension of the framework to viscous flows. In addition, more complex interactions of bubbles and droplets and drop-wall interactions will be addressed. Detailed investigations on the implicit-explicit framework are currently underway.

Acknowledgements C. Müller and J. Zeifang were supported by the German Research Foundation (DFG) through the project GRK 2160/1 “Droplet Interaction Technologies”. S. Jöns was supported by the DFG through the project SFB-TRR 75, Project number 84292822 - “Droplet Dynamics Under Extreme Ambient Conditions” and C.-D. Munz by the DFG under Germany’s Excellence Strategy - EXC 2075 - 390740016. The simulations were performed on the national supercomputer Cray XC40 (Hazel Hen) at the High Performance Computing Center Stuttgart (HLRS) under the grant numbers *hpcmphas/44084*.

References

1. Aslam, T.D.: A partial differential equation approach to multidimensional extrapolation. J. Comput. Phys. **193**(1), 349–355 (2004). https://doi.org/10.1016/j.jcp.2003.08.001
2. Beck, A.D., Bolemann, T., Flad, D., Frank, H., Gassner, G.J., Hindenlang, F., Munz, C.D.: High-order discontinuous Galerkin spectral element methods for transitional and turbulent flow simulations. Int. J. Numer. Methods Fluids **76**(8), 522–548 (2014)
3. Carpenter, M., Kennedy, C.: Fourth-order $2N$-storage Runge-Kutta schemes. Technical report, NASA Langley Research Center (1994)
4. Castro, M., Gallardo, J., Parés, C.: High order finite volume schemes based on reconstruction of states for solving hyperbolic systems with nonconservative products. Applications to shallow-water systems. Mat. Comput. **75**(255), 1103–1134 (2006)
5. Chandran, J., Salih, A.: A modified equation of state for water for a wide range of pressure and the concept of water shock tube. Fluid Phase Equilib. **483**, 182–188 (2019)

6. du Chéné, A., Min, C., Gibou, F.: Second-order accurate computation of curvatures in a level set framework using novel high-order reinitialization schemes. J. Sci. Comput. **35**(2–3), 114–131 (2007). https://doi.org/10.1007/s10915-007-9177-1
7. Denner, F., van Wachem, B.G.: Numerical time-step restrictions as a result of capillary waves. J. Comput. Phys. **285**, 24–40 (2015)
8. Dumbser, M., Loubère, R.: A simple robust and accurate a posteriori sub-cell finite volume limiter for the discontinuous Galerkin method on unstructured meshes. J. Comput. Phys. **319**, 163–199 (2016). https://doi.org/10.1016/j.jcp.2016.05.002
9. Einfeldt, B.: On Godunov-type methods for gas dynamics. SIAM J. Numer. Anal. **25**(2), 294–318 (1988). https://doi.org/10.1137/0725021
10. Fechter, S.: Compressible multi-phase simulation at extreme conditions using a discontinuous galerkin scheme (2015). https://doi.org/10.18419/opus-3982
11. Fechter, S., Jaegle, F., Schleper, V.: Exact and approximate Riemann solvers at phase boundaries. Comput. Fluids **75**, 112–126 (2013). https://doi.org/10.1016/j.compfluid.2013.01.024
12. Fechter, S., Munz, C.D.: A discontinuous Galerkin-based sharp-interface method to simulate three-dimensional compressible two-phase flow. Int. J. Numer. Meth. Fluids **78**(7), 413–435 (2015). https://doi.org/10.1002/fld.4022
13. Fedkiw, R.P., Aslam, T., Merriman, B., Osher, S.: A non-oscillatory Eulerian approach to interfaces in multimaterial flows (the ghost fluid method). J. Comput. Phys. **152**(2), 457–492 (1999). https://doi.org/10.1006/jcph.1999.6236
14. Föll, F., Hitz, T., Müller, C., Munz, C.D., Dumbser, M.: On the use of tabulated equations of state for multi-phase simulations in the homogeneous equilibrium limit. Shock Waves (2019). https://doi.org/10.1007/s00193-019-00896-1
15. Fuster, D., Popinet, S.: An all-mach method for the simulation of bubble dynamics problems in the presence of surface tension. J. Comput. Phys. **374**, 752–768 (2018)
16. Grooss, J., Hesthaven, J.: A level set discontinuous Galerkin method for free surface flows. Comput. Methods Appl. Mech. Eng. **195**(25–28), 3406–3429 (2006). https://doi.org/10.1016/j.cma.2005.06.020
17. Hindenlang, F., Gassner, G.J., Altmann, C., Beck, A., Staudenmaier, M., Munz, C.D.: Explicit discontinuous Galerkin methods for unsteady problems. Comput. Fluids **61**, 86–93 (2012). https://doi.org/10.1016/j.compfluid.2012.03.006
18. Huerta, A., Casoni, E., Peraire, J.: A simple shock-capturing technique for high-order discontinuous Galerkin methods. Int. J. Numer. Meth. Fluids **69**(10), 1614–1632 (2011). https://doi.org/10.1002/fld.2654
19. Jiang, G.S., Peng, D.: Weighted ENO schemes for Hamilton-Jacobi equations. SIAM J. Sci. Comput. **21**(6), 2126–2143 (2000). https://doi.org/10.1137/s106482759732455x
20. Jolgam, S., Ballil, A., Nowakowski, A., Nicolleau, F.: On equations of state for simulations of multiphase flows. In: Proceedings of the World Congress on Engineering 2012. 4–6 July 2012. London, UK., vol. 3, pp. 1963–1968 (2012)
21. Kennedy, C.A., Carpenter, M.H.: Additive Runge-Kutta schemes for convection–diffusion–reaction equations. Appl. Numer. Math. **44**(1–2), 139–181 (2003). https://doi.org/10.1016/s0168-9274(02)00138-1
22. Knoll, D.A., Keyes, D.E.: Jacobian-free Newton-Krylov methods: a survey of approaches and applications. J. Comput. Phys. **193**(2), 357–397 (2004)
23. Kopriva, D.A.: Spectral element methods. In: Scientific Computation, pp. 293–354. Springer Netherlands (2009). https://doi.org/10.1007/978-90-481-2261-5_8
24. Krais, N., Beck, A., Bolemann, T., Frank, H., Flad, D., Gassner, G., Hindenlang, F., Hoffmann, M., Kuhn, T., Sonntag, M., Munz, C.D.: FLEXI: A high order discontinuous Galerkin framework for hyperbolic-parabolic conservation laws. Comput. Math. with Appl. (2020). https://doi.org/10.1016/j.camwa.2020.05.004
25. Lervag, K.Y.: Calculation of interface curvature with the level-set method. arXiv preprint arXiv:1407.7340 (2014)
26. Lervag, K.Y., Müller, B., Munkejord, S.T.: Calculation of the interface curvature and normal vector with the level-set method. Comput. Fluids **84**, 218–230 (2013). https://doi.org/10.1016/j.compfluid.2013.06.004

27. Liu, T., Khoo, B., Wang, C.: The ghost fluid method for compressible gas–water simulation. J. Comput. Phys. **204**(1), 193–221 (2005). https://doi.org/10.1016/j.jcp.2004.10.012
28. Liu, T., Khoo, B., Xie, W.: The modified ghost fluid method as applied to extreme fluid-structure interaction in the presence of cavitation. Commun. Comput. Phys. **1**(5), 898–919 (2006)
29. Liu, T.G., Khoo, B.C., Wang, C.W.: The ghost fluid method for compressible gas-water simulation. J. Comput. Phys. **204**(1), 193–221 (2005). https://doi.org/10.1016/j.jcp.2004.10.012
30. Marchandise, E., Remacle, J.F.: A stabilized finite element method using a discontinuous level set approach for solving two phase incompressible flows. J. Comput. Phys. **219**(2), 780–800 (2006). https://doi.org/10.1016/j.jcp.2006.04.015
31. Müller, C., Hitz, T., Jöns, S., Zeifang, J., Chiocchetti, S., Munz, C.D.: Improvement of the level-set ghost-fluid method for the compressible Euler equations. In: Lamanna, G., Tonini, S., Cossali, G.E., Weigand, B. (eds.) Droplet Interaction and Spray Processes. Springer, Heidelberg, Berlin (2020)
32. Nourgaliev, R.R., Dinh, T.N., Theofanous, T.G.: Adaptive characteristics-based matching for compressible multifluid dynamics. J. Comput. Phys. **213**(2), 500–529 (2006)
33. Persson, P.O., Peraire, J.: Sub-cell shock capturing for discontinuous Galerkin methods. In: 44th AIAA Aerospace Sciences Meeting and Exhibit. American Institute of Aeronautics and Astronautics (2006). https://doi.org/10.2514/6.2006-112
34. Saurel, R., Cocchi, J.P., Butler, P.B.: Numerical study of cavitation in the wake of a hypervelocity underwater projectile. J. Propuls. Power **15**(4), 513–522 (1999). https://doi.org/10.2514/2.5473
35. Saurel, R., Petitpas, F., Abgrall, R.: Modelling phase transition in metastableliquids: application to cavitating and flashing flows. J. Fluid Mech. **607** (2008). https://doi.org/10.1017/s0022112008002061
36. Schleper, V.: A HLL-type Riemann solver for two-phase flow with surface forces and phase transitions. Appl. Numer. Math. **108**, 256–270 (2016). https://doi.org/10.1016/j.apnum.2015.12.010
37. Sethian, J.A.: A fast marching level set method for monotonically advancing fronts. Proc. Natl. Acad. Sci. **93**(4), 1591–1595 (1996)
38. Sonntag, M.: Shape derivatives and shock capturing for the Navier-Stokes equations in discontinuous Galerkin methods. Dissertation, University of Stuttgart (2017)
39. Sonntag, M., Munz, C.D.: Efficient parallelization of a shock capturing for discontinuous Galerkin methods using finite volume sub-cells. J. Sci. Comput. **70**(3), 1262–1289 (2016). https://doi.org/10.1007/s10915-016-0287-5
40. Sussman, M., Smereka, P., Osher, S.: A level set approach for computing solutions to incompressible two-phase flow. J. Comput. Phys. **114**(1), 146–159 (1994). https://doi.org/10.1006/jcph.1994.1155
41. Tanguy, S., Berlemont, A.: Application of a level set method for simulation of droplet collisions. Int. J. Multiph. Flow **31**(9), 1015–1035 (2005)
42. Toro, E.F., Spruce, M., Speares, W.: Restoration of the contact surface in the HLL-Riemann solver. Shock Waves **4**(1), 25–34 (1994). https://doi.org/10.1007/bf01414629
43. Tsai, Y.H.R., Cheng, L.T., Osher, S., Zhao, H.K.: Fast sweeping algorithms for a class of Hamilton-Jacobi equations. SIAM J. Numer. Anal. **41**(2), 673–694 (2003)
44. Vahab, M., Miller, G.: A front-tracking shock-capturing method for two gases. Commun. Appl. Math. Comput. Sci. **11**(1), 1–35 (2015)
45. Wang, C.W., Liu, T.G., Khoo, B.C.: A real ghost fluid method for the simulation of multimedium compressible flow. SIAM J. Sci. Comput. **28**(1), 278–302 (2006). https://doi.org/10.1137/030601363
46. Wardlaw Jr., A.B., Luton, J.A.: Fluid-structure interaction mechanisms for close-in explosions. Shock. Vib. **7**(5), 265–275 (2000)
47. Wardlaw Jr., A.B., Mair, H.U.: Spherical solutions of an underwater explosion bubble. Shock. Vib. **5**(2), 89–102 (1998)
48. Williamson, J.H.: Low-storage Runge-Kutta schemes. J. Comput. Phys. **35**, 48–56 (1980)

49. Winter, J.M., Kaiser, J.W., Adami, S., Adams, N.A.: Numerical investigation of 3D drop-breakup mechanisms using a sharp interface level-set method. In: 11th International Symposium Turbulence Shear Flow Phenomena, TSFP 2019 (2001), pp. 1–6 (2019)
50. Zeifang, J., Kaiser, K., Beck, A., Schütz, J., Munz, C.D.: Efficient high-order discontinuous Galerkin computations of low Mach number flows. Commun. Appl. Math. Comput. Sci. **13**(2), 243–270 (2018)
51. Zeifang, J., Schütz, J., Kaiser, K., Beck, A., Lukacova-Medvid'ova, M., Noelle, S.: A novel full-Euler low Mach number IMEX splitting. Commun. Comput. Phys. **27**(1), 292–320 (2019). https://doi.org/10.4208/cicp.OA-2018-0270
52. Zheng, H.W., Shu, C., Chew, Y.T., Qin, N.: A solution adaptive simulation of compressible multi-fluid flows with general equation of state. Int. J. Numer. Methods Fluids **67**(5), 616–637 (2011). https://doi.org/10.1002/fld.2380